Effects of varying Al_x moles on the structure and luminescence properties of $ZnAl_xO_{1.5x+1}$:0.1% Tb^{3+} nanophosphor prepared using citrate sol-gel method

V.M. Maphiri[a*], L.T. Melato[b], M.R. Mhlongo[a], T.T. Hlatshwayo[c], T.E. Motaung[d,e], L.F. Koao[f], S.V. Motloung[a,g**]

[a]Department of Physics, Sefako Makgatho Health Science University, P. O. Box 94, Medunsa, 0204, South Africa
[b]Department of Mathematics, Non Destructive Testing and Physics, Vaal University of Technology, Andries Potgieter Blvd, Vanderbijlpark, 1900, South Africa
[c]Department of Physics, University of Pretoria, Pretoria, 0002, South Africa
[d]Department of Chemistry, School of Science in the College of Science Engineering and Technology, University of South Africa, Preller Street, Muckleneuk Ridge, City of Tshwane, P. O Box 392, UNISA 0003, South Africa
[e]Department of Chemistry, Sefako Makgatho Health Science University, P. O. Box 94, Medunsa, 0204, South Africa
[f]Department of Physics, University of the Free State (Qwaqwa Campus), Private Bag X13, Phuthaditjhaba 9866, South Africa
[g]Department of Chemical and Physical Sciences, Walter Sisulu University, Mthatha, South Africa

***Corresponding author**: * V.M. Maphiri (vusanimuswamaphiri@gmail.com) and **S.V. Motloung (cchataa@gmail.com)

Foundation item: Project supported by the South African National Research Foundation (NRF) Thuthuka programme (fund number: UID 99266 and 113947), NRF incentive funding for rated researchers (IPRR) (Grant No: 114924) and NRF Black Academics Advancement Programme (BAAP) (Grant No: 138233).

Highlights

- $ZnAl_xO_{1.5x+1}$:0.1% Tb^{3+} ($0.25 \leq x \leq 5.0$) nano-powders were synthesized via citrate sol–gel method.
- For the $x < 1.5$, the samples crystal structure consists of mixed phases of the cubic $ZnAl_2O_4$ and hexagonal ZnO phases.PL emission colour and intensity highly depend on the Tb^{3+} environment within the $ZnAl_2O_4$ matrix.
- The prepared nano-powders have similar decay mechanism.
- Emission colour can be tuned from blue to green by varying the Al_x moles.

Abstract. Un-doped and $ZnAl_xO_{1.5x+1}$:0.1% Tb^{3+} (ZAOT) nano-powders were synthesized via citrate sol-gel method. The Al_x moles were varied in the range of $0.25 \leq x \leq 5.0$. The X-ray powder diffraction (XRD) data reveal that for $x < 1.5$, the prepared samples crystal structure consists of mixed phases of the cubic $ZnAl_2O_4$ and hexagonal ZnO phases, while for $x \geq 1.5$ the structure consists of single phase of cubic $ZnAl_2O_4$. The Raman and Fourier-Transform Infrared (FTIR) vibrational spectroscopy shows the presence of vibrations emanating $ZnAl_2O_4$ spinel. Scanning electron microscopy (SEM) and Transmission electron microscopy (TEM) shows the presence of irregular sphere at $x \geq 2.0$ attributed to $ZnAl_2O_4$.

The photoluminescence (PL) spectroscopy revealed emissions from both the host and Tb^{3+} transitions. Emissions from Tb^{3+} are observed at 382, 414, 439, 458 and 489, 545, 585, 621 nm, which are attributed to the $^5D_3 \rightarrow {}^7F_{6,5,4,2}$ and $^5D_4 \rightarrow {}^7F_{6,5,4,3}$, respectively. The results confirmed that the Tb^{3+} occupation site depend on the Al_x moles. The International Commission on Illumination (CIE) colour chromaticity shows that the emission colour could be tuned from blue to green by varying the Al_x moles.

Graphically abstract

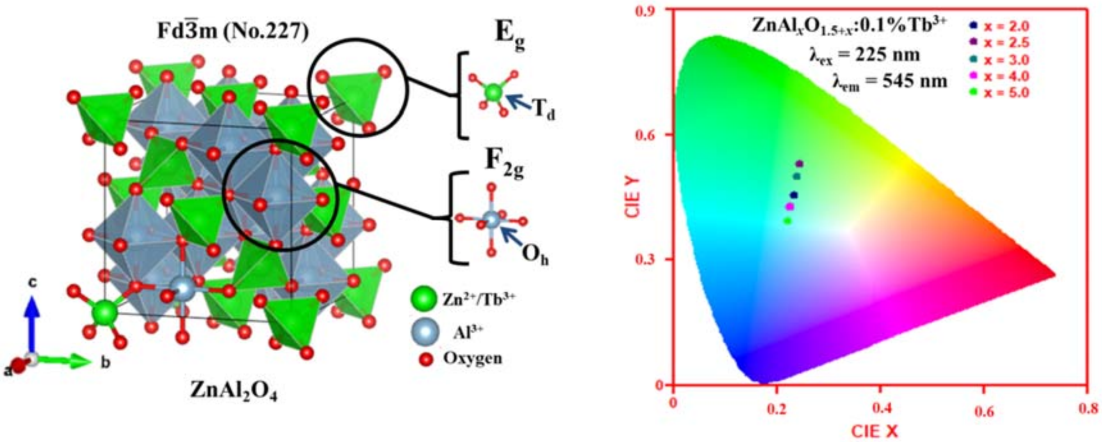

The polyhedron unit cell of $ZnAl_2O_4$ with schematic depicting the elemental occupation together with the obtained emission colour at Alx moles ($2.0 \leq x \leq 5.0$)

Keywords: Citrate sol-gel; $ZnAl_2O_4$/ZnO; Tb^{3+}-doped; Al_x moles; photoluminescence

1. Introduction

In the past few decades, metal oxides (MO) have enticed many researches in different fields due to their unique physical and chemical properties [1]. MO are on the cutting edge of technology in various field of science such as water splitting [2–4], energy storage and conversions [5,6], photoluminescence (PL) [7–9] and transparent conducting oxide [1,10,11]. This is mainly due to their band gap located directly at the gamma (Γ) point which was determined theoretically and experimentally to be around few electron volts (eV) [12–14]. The MO denoted by the AB_2O_4 formula are usually referred to as spinel contains around 120 compound members with $ZnAl_2O_4$ (zinc aluminate or gahnite) being one of the most investigated host material [1,9,15,16]. $ZnAl_2O_4$ is well known to crystallizes in the cubic crystal structures of the $Fd\bar{3}m$ space group, where Zn and Al respectively occupies the tetrahedral (T_d) and octahedral (O_h) sites in the crystal matrix while oxygen atoms occupies the Wyckoff 32e position located at (u, u, u), where $u \approx 0.25$ [1,17,18]. The above-mentioned formation is referred to as normal $(Zn)[Al]_2O_4$ configuration. Several studies have shown a sight inverted $(ZnAl)[ZnAl]_2O_4$ configuration where the T_d (denoted by parentheses) and O_h [denoted by bracket] are shared amongst the Zn and Al ions [17–20]. The positioning of the atoms or the structural configuration of the $ZnAl_2O_4$ has been shown to depends on synthesis parameter such as the temperature. $ZnAl_2O_4$ have shown great potential application in glass ceramic and photoelectronic devices [21,22]. Some spinel such as $NiFe_2O_4$ and $CoFe_2O_4$ [5,17,21] can crystallise in inversion configurations where di – and tri – valent ion occupies the O_h and T_d sites. Raman spectroscopy has been an wonderful technique of detecting such behaviours [18–20].

Various studies have been conducted on $ZnAl_2O_4$ to optimize and tune the emission colour. Most researchers introduce foreign ions (i.e. dopants) mostly form the rare earths within the $ZnAl_2O_4$ spinel at various doping concentrations [7–9,22–24]. Trivalent terbium ion (Tb^{3+}) is one of the most explored dopant due to its emission broadband covering the entire visible wavelength with an intense green emission colour around 525 – 560 nm due to the $^5D_4 \rightarrow {}^7F_5$ magnetic dipole (MD) transition which is known to hardly varies in different in crystal field environment [22–26]. Linganna et al. [27] have shown that the emission colour of Tb^{3+} ion can be change due to the presence of various crystal field environment. This phenomenon can be attributed to the increase and decrease of the $^5D_4 \rightarrow {}^7F_5$ electrical dipole (ED) transition emission intensity which is sensitive to the local environment and depends on the symmetry of the crystal field; in asymentric enviroment the intensity of this peak is higher as compared to in symmetric enviroment which drastical impact the emission colour. However, other studies optimize and tune the emission colour by triply, doubly, and singly doping Tb^{3+} with other dopants within the $ZnAl_2O_4$ matrix [22–24,28–32]. Refs [22–24,26,29] shows a successful incorporation of Tb^{3+} and other dopants within the $ZnAl_2O_4$ matrix which led to some astonishing results such as; the possibility of a full – colour field emission from the doped $ZnAl_2O_4$ and the presence of two energy transfer (ET) system. The intra – ET within Tb^{3+} ions and between Tb^{3+} to Mn^{2+}, which were described as follows Tb^{3+} ($^5D_3$) + Tb^{3+} ($^7F_6$) → Tb^{3+} ($^5D_4$) + Tb^{3+} ($^7F_{2,1,0}$) and $Tb^{3+} \rightarrow Mn^{2+}$[23], respectively. The intra – ET happened via overlapping of the Tb^{3+} band and ET between Tb and Mn happened via the absorption of excitation energy at 350 nm from Tb^{3+} by the 654 nm emission peak of Mn^{2+} transitions. Most of the reported work on $ZnAl_2O_4$ focuses on the varying the dopant/s concentration [22–24,26,28–32] and synthesis conditions [16,25,29,33–35]. Only a few studies reported the effect of the host constitution element concentration [36–39]. Our group has previous reported; the effect of the Mg_x moles on the $Mg_xAl_2O_{3+x}$: 0.88% Cd^{2+} ($0.25 \leq x \leq 4.5$) system [15] and interchanging Ba and Zn within $Ba_{1-x}Zn_xAl_2O_4$:0.1% Eu^{3+} ($0 \leq x \leq 1$) [9]. The XRD results showed that the structural phase changes from $MgAl_2O_4$ to MgO occurred at $x = 2.5$ ($Mg_{2.5}$) and PL also changed based on the concentration of Mg_x moles. While the XRD of $Ba_{1-x}Zn_xAl_2O_4$:0.1% Eu^{3+} shows single phase of $BaAl_2O_4$ and $ZnAl_2O_4$ at $x \leq 0.2$ and $x = 1.0$, respectively.

The effect of Al_x moles on the structure and luminescence properties of $ZnAl_xO_{1.5x+1}$:0.1% Tb^{3+} (ZAOT) ($0.25 \leq x \leq 5.0$) has not been reported in literature to date. Thus, this study explores the influence of varying the Al_x moles on the structure, morphology, and PL properties with the aim of producing alternative phosphor material for the practical application such as on the lighting emitting devices (LEDs) particularly the bluish and greenish colour emitting LEDs. The results showed that the variation on the structural and luminescence properties highly depends on the Al_x moles. The emission intensity depends on the phases present and Tb^{3+} site occupation, which is regulated by the Al_x moles. The observed emission pathways are also proposed.

2. Experimental

2.1. Synthesis

The $ZnAl_xO_{1.5x+1}$:0.1% Tb^{3+} ($0.25 \leq x \leq 5.0$) series was synthesized via citrate sol-gel technique. The materials were prepared by dissolving stoichiometric masses of zinc nitrates hexa-hydrate ($Zn(NO_3)_2 \cdot 6H_2O$, 99.9%] corresponding to 1 mole while aluminium nitrates nano-hydrate [$Al(NO_3)_3 \cdot 9H_2O$, 98.5%] was added at the range of $0.25 \leq x \leq 5.0$ moles; citric acid (CA) [$C_6H_8O_7 \cdot H_2O$, 99%] was also dissolved in deionized water (prepared using DRAWELL, laboratory water purification system) to chelate and stabilize the solution [34,40]. The stoichiometric molar ratios of Zn:CA was kept constant at 1:0.75 for all the prepared samples while varying the moles of Al^{3+}. A specified amount of terbium nitrate penta-hydrate [$Tb(NO_3)_3 \cdot 5H_2O$, 99.9%] was added to dope with 0.1% Tb^{3+}. All the chemicals used in this study were purchased at Germany's Sigma-Aldrich. The solution was heated at ~ 80 ^oC while constantly stirring using the magnetic stirrer until the gels were formed. The gels were dried for 12 h in room temperature and subsequently annealed at 1000 ^oC in a furnace (carbolite gero, United Kingdom, CWF 1300 furnace) for 1 h. The resulting solid-like-foam products were ground into fine powder samples using the pestle and mortar.

2.2.Characterization

The powder samples were analyzed with the Bruker D8-Advance X-ray powder diffraction (XRD) (USA) with a CuKα (1.5405 Å) radiation, WITec 300 RAS+ confocal Raman microscopy (Germany) using the 532 nm at 2 mW and Bruker Alpha platinum-ATR Fourier-transform infrared spectroscopy (FTIR) (USA) in the range of 400 to 1000 cm^{-1} was used to analyze the crystal structure, phase, functional group, and the vibration bands. The structural phase from the XRD were identified using X'pert Highscore plus software (United Kingdom) and the relative phase quantification (%) were estimated using the Rietveld method. The particle shape, surface morphology and elementary constituents were characterized by the Zeiss Supra 55 scanning electron microscope (SEM) at 20 kV coupled with an energy dispersive X-ray spectroscope (EDS) (Japan). Crystallite shape and sizes was analysed via the JEOL JEM 1010 transmission electron microscopy (TEM) (Japan). The room temperature photoluminescence (PL) spectra and lifetime measurements were performed by the Hitachi F-7000 fluorescence spectrophotometer (Japan) using a 150 W monochromatized Xenon lamp as an excitation source.

3. Results and discussion

3.1. X-ray powder diffraction

The XRD patterns of the prepared samples are shown on Fig. 1. These diffraction patterns are polycrystalline and could be indexed to the standard patterns of the hexagonal ZnO (JCPDS 80-80075 and space group P63mc No. 186) and cubic $ZnAl_2O_4$ (JCPDS 82-1043 and space group Fd$\bar{3}$m No. The unit cells of both the ZnO and $ZnAl_2O_4$ created using VESTA software (Ver. 3.5.2, 64-bit Edition) and crystallographic information files corresponding to the P63mc No. 186 and Fd$\bar{3}$m No. 227 space group are shown in Fig. 2 (a) and (b), respectively. The quantification percentages of these phases are shown on Table 1. From Fig. 1, the results show that the ZnO phase quantity decreased with an increase in Al_x moles up to x = 1.0, while the $ZnAl_2O_4$ phase quantity increased as Al_x moles was increased. $ZnAl_2O_4$ phase quantity reached 100 % at $x \geq 1.0$. The results showed that at a lower Al_x moles of $x < 1.5$, the XRD patterns consists of the mixed phases of both the hexagonal ZnO and cubic $ZnAl_2O_4$. This observation is attributed to the insufficient Al atoms to bond with the Zn atoms to completely form $ZnAl_2O_4$. This led to the excess Zn^{2+} which easily reacts with O^{2-} to form ZnO. Similar XRD with both ZnO and $ZnAl_2O_4$ phases has been reported in Refs [18,25]. When $x \geq 1.5$ the results suggest that the samples constitute of only cubic $ZnAl_2O_4$ phase, which is attributed to enough Al atoms available to completely form $ZnAl_2O_4$ in a solution. These results suggest that the transition from dual $ZnAl_2O_4$/ZnO mixed phases to $ZnAl_2O_4$ single phase occurred in a range of Al_x moles is $1 \leq x < 1.5$. Thus, the mixed phase/s in ZAOT highly depends on the Al_x moles. The XRD patterns of the doped (x = 2.0) and un-doped (x = 2.0*) are similar, signifying a successful incorporation of Tb^{3+} within the $ZnAl_2O_4$ crystal lattice.

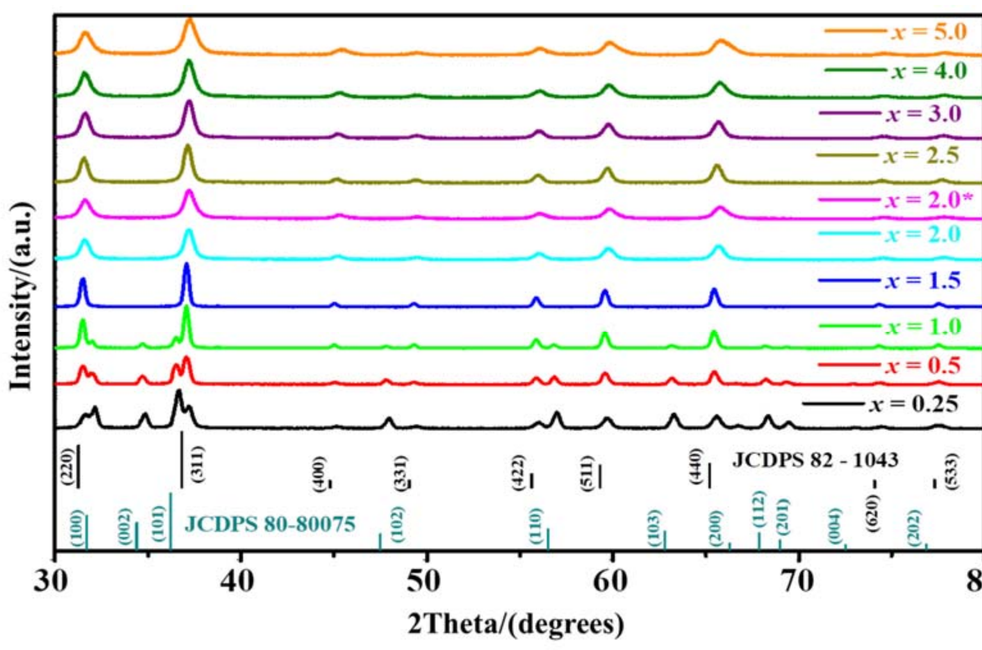

Fig. 1 The XRD pattern of the x = 2.0* (un-doped $ZnAl_2O_4$) and $ZnAl_xO_{1.5x+1}$:0.1% Tb^{3+} ($0.25 \leq x \leq 5.0$) nanopowders.

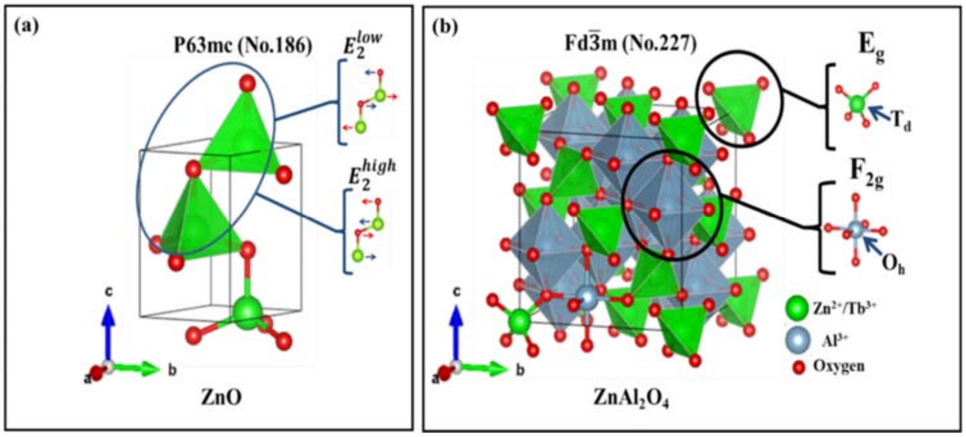

Fig. 2 Unit cell of the (a) ZnO and (b) $ZnAl_2O_4$ with atom vibrational schematic.

Analysis of the most intense diffraction peaks (101) and (311) from ZnO and $ZnAl_2O_4$ phase are shown on Fig. 3. Fig. 3 (a) shows the decrease of the ZnO (101) diffraction peak intensity with an increase of Al_x moles and completely disappears at $x > 1.5$, signifying the total removal of the ZnO phase. The increase of the $ZnAl_2O_4$ (311) diffraction peak intensity as Al_x moles increases suggest an increase in the crystallinity (or formation) of the $ZnAl_2O_4$ phase. This is due to the availability of enough Al atoms to completely form $ZnAl_2O_4$ single phase.

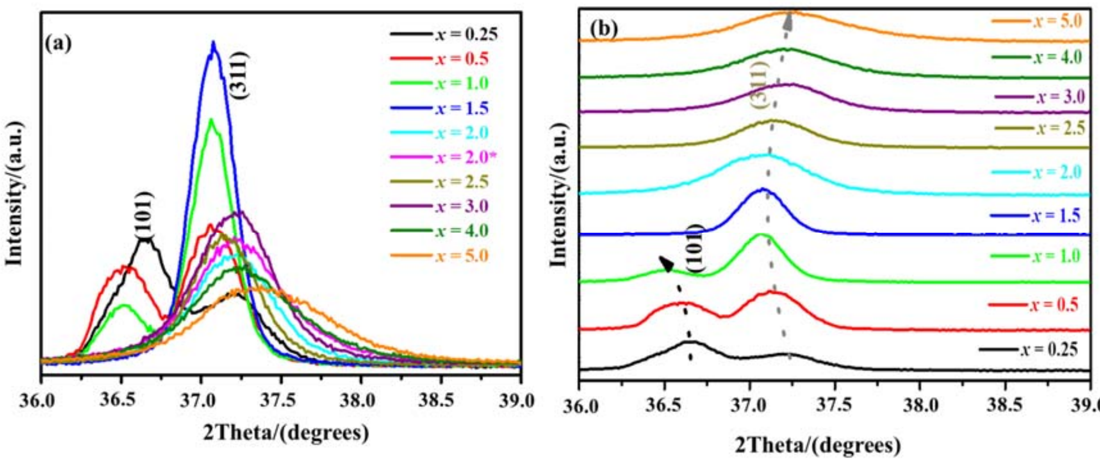

Fig. 3 Analysis of diffraction peak (a) intensities and (b) shift of the (101) ZnO and (311) $ZnAl_2O_4$ phase of $ZnAl_xO_{1.5x+1}$:0.1% Tb^{3+} ($0.25 \leq x \leq 5.0$).

The stacked analysis of the ZnO (101) and $ZnAl_2O_4$ (311) displayed on Fig. 3 (b) shows that both peaks have shifted towards a lower diffraction angle for $x \leq 1.5$ suggesting an increased lattice constant [9,15]. On the $ZnAl_2O_4$ phase, the lattice increased due to the occupation of excess Zn^{2+} (ionic radius = 0.74 Å [9,41]) within the Al^{3+} (ionic radius = 0.53 Å [7,41]) site in the $ZnAl_2O_4$ crystal lattice. As for the ZnO phase, the lattice constant increases due to the incorporation of Al^{3+} ions forming octahedral holes within the ZnO matrix which pave the formation of single phase $ZnAl_2O_4$. Note that octahedral holes (voids or occupation site) are larger than tetrahedral holes. Thus, this result in an expansion of the lattice parameter. When $x \geq 1.5$, the (311) diffraction peak broadens and shifts towards higher diffraction angle signifying a decrease in lattice constant. Meaning that some of the Al^{3+} are occupying the

Zn^{2+} sites [42,43]. The lattice constant of the $ZnAl_2O_4$ and ZnO were estimated using the equation (1) [9,12] and (2) [9,44], respectively.

$$\frac{1}{d_{hkl}^2} = \frac{h^2+k^2+l^2}{a^2} \quad \ldots (1)$$

$$\frac{1}{d_{hkl}^2} = \frac{4}{3}\left(\frac{h^2+hk+k^2}{a^2} + \frac{l^2}{C^2}\right) \quad \ldots (2)$$

where a and c are the lattice constant, d is the interplanar distance and hkl are the miller indices. The lattice constant (a) for $ZnAl_2O_4$ were calculated from the (311) diffraction peaks. The lattice constant (a) and (c) for ZnO were calculated from the (002) and (101) diffraction peaks, respectively. The estimated lattice constant for both the ZnO and $ZnAl_2O_4$ are presented in Table 1. The obtained values are in agreement with those previously reported values in literature by the Refs [25,44–46]. The average lattice constants $a = b$ and c for ZnO are 2.836 and 5.158 Å, respectively, and $ZnAl_2O_4$ average lattice constants is $a = b = c$ = 8.011 Å. The $ZnAl_2O_4$ lattice constant as a function of Al_x moles is depicted on Fig. S1 (a) (supplementary information). The lattice constant increase from x = 0.25 to 1 due to the excess of Zn atoms compared to Al atoms. The dramatic decrease to x = 1.5 is due to the completely removal of ZnO phase due to reasonable Zn:Al ratio to start forming $ZnAl_2O_4$ single phase. An increase in lattice parameters from x = 1.5 to 2.5 might be attributed to the full formation of stable $ZnAl_2O_4$ single phase. The observed decrease in lattice parameter at x > 2.5 is possibly due to the Al^{3+} occupying the Zn^{2+} ions in $ZnAl_2O_4$ crystal lattice. This can be further motivated by the absence of alumina (Al_2O_3) related diffraction patterns in Fig. 1 and Table 1. These results are consistence with the $Mg_xAl_2O_4$:0.88% Cd^{2+} ($0.25 \leq x \leq 4.5$) system [15], which showed that an increasing in the Mg^{2+} ions transformed the $MgAl_2O_4$ structure to MgO.

The crystallite size for the ZnO and $ZnAl_2O_4$ were estimated from the dominant diffraction peaks ZnO (101) and $ZnAl_2O_4$ (311) using Scherrer's formula equation S1 [47]. The estimated values are presented in Table 1 and the crystallite size of the $ZnAl_2O_4$ as a function of Al_x mole is presented in Fig. S1 (a). The graph of crystallite resembles a similar behaviour as that of the lattice constant. The strain on the $ZnAl_2O_4$ and ZnO phases were calculated from Williamson and Hall method [48], and the values are presented in Table 1. The strain for the $ZnAl_2O_4$ as a function of the Al_x is shown on Fig. S1 (b). When $0.25 \geq x > 1.0$ the strain decreases due to incorporation of smaller ionic radius Al^{3+} ions within the ZAOT system. At x = 1.5, the strain increases due to the formation of $ZnAl_2O_4$ single phase. At $1.5 < x < 2.5$, the decrease in strain is probably due to easy incorporation of Al^{3+} ions into $ZnAl_2O_4$. Above $x \geq 2.5$, the strain increases linearly as it becomes more difficult to incorporate more Al^{3+} ions into the $ZnAl_2O_4$ matrix.

Table 1. Sample identification, strain, lattice constant and crystallites size of ZnO and $ZnAl_2O_4$.

Sample ID	Quantification (%)		Lattice parameter (Å)			Crystallite Size (nm)		Strain (%)	
x	ZnO	$ZnAl_2O_4$	ZnO		$ZnAl_2O_4$	ZnO	$ZnAl_2O_4$	ZnO	$ZnAl_2O_4$
			***a*(Å)**	***c*(Å)**	***a*(Å)**				
0.25	47.6	52.4	2.830	5.147	8.003	22	20	0.0182	0.0223
0.5	30.8	69.2	2.839	5.163	8.033	25	23	0.0156	0.0189
1.0	13.7	86.3	2.839	5.164	8.036	24	30	0.0166	0.0148
1.5	-	100	-	-	8.003	-	13	-	0.0323
2.0	-	100	-	-	8.010	-	16	-	0.0267
2.0*	-	100	-	-	8.033	-	30	-	0.0144
2.5	-	100	-	-	8.020	-	18	-	0.0240
3.0	-	100	-	-	8.006	-	16	-	0.0279
4.0	-	100	-	-	7.996	-	13	-	0.0342
5.0	-	100	-	-	7.970	-	10	-	0.0407

* denotes un-doped sample

3.2. Raman Spectroscopy

Raman spectroscopy was employed to identify the molecular structure of the prepared pure phase samples and the obtained spectra are shown on Fig. 4. The results show that there are three Raman peaks located at 62, 420 and 660 cm^{-1}. The Raman peaks at around 420 and 660 cm^{-1} are due to $ZnAl_2O_4$ [17,18]. It is generally accepted that Raman modes within the medium frequency range (300-600 cm^{-1}) modes are due to the MO_6 octahedral while the high range frequency (> 600 cm^{-1}) modes are due to the MO_4 tetrahedral. Thus, the 420 and 660 cm^{-1} bands can be attributed to the E_g and F_{2g} mode ascribed to the O_h and T_d site [19,20] as shown in Fig. 2 (b), respectively. These observed two peaks from $ZnAl_2O_4$ is in good agreement with the previous reports [17–20]. Previous studies [17,49] have shown that E_g and F_{2g} modes of Raman spectrum of the inverse spinel occurred in the 350 - 400 and 490 - 640 cm^{-1} region. $Zn_{0.9}Cu_{0.1}Al_2O_4$ and $Zn_{0.9}Ni_{0.1}Al_2O_4$ have also shown a lower frequency Raman shift located in the 395-410 and 630-650 cm^{-1} which was attributed to appearance of minor inverse spinel [17,19]. Therefore, these results suggest that the prepared $ZnAl_2O_4$ spinel has crystallised in the normal configuration. The Raman peak located at 62 cm^{-1} can be attributed to the Zn interstitial [50] and/or the presents of Tb^{3+} within the $ZnAl_2O_4$ hosts matrix. The Raman confirms the presence of $ZnAl_2O_4$ single phase for the $x \geq 2$ samples. Note that the intensity of the Raman peak at 62 cm^{-1} for the $x = 2.0$ (un-doped) sample is lower than the doped sample, which suggest that the Zn interstitial sites are more pronounced for the doped compared to the un-doped sample [43]. Thus, the presence of Tb^{3+} within the $ZnAl_2O_4$ has an influence on this Raman peak intensity. Based on the XRD (Fig. 1) and Raman (Fig. S2) results, it is therefore reasonable to exclude the samples with Al content ($x < 2.0$) in further structural and spectroscopic analysis because they consist of dual phase.

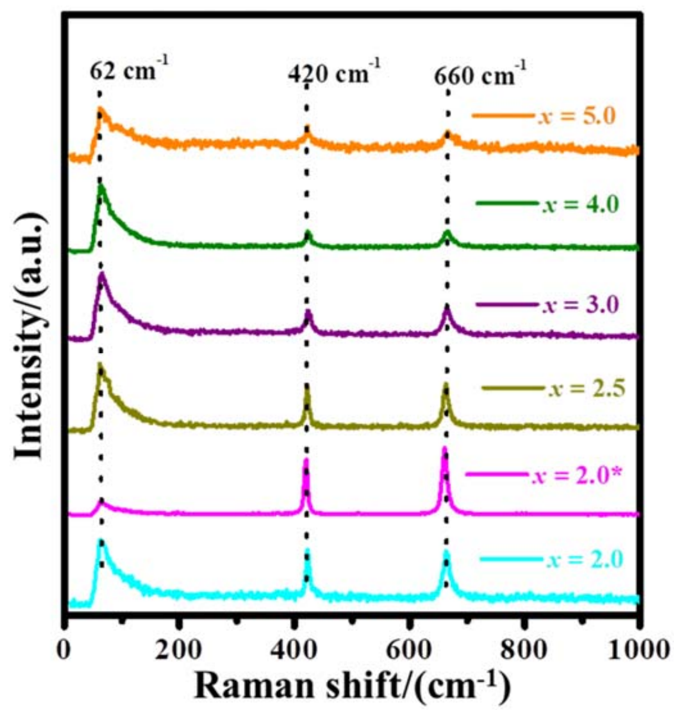

Fig. 4 Spectra for the $x = 2.0$* (un-doped $ZnAl_2O_4$) and $ZnAl_xO_{1.5x+1}$:0.1% Tb^{3+} ($2.0 \leq x \leq 5.0$).

To further investigate the structural effects of Al_x moles on the $ZnAl_2O_4$ phases, the zoomed version of the E_g (O_h of $ZnAl_2O_4$) Raman peaks within the range of 390 – 470 cm^{-1} is shown in Fig. S3. The shift to higher wavenumber of the E_g with an increase in Al_x suggest that the Al^{3+} might be substituting the Zn^{2+} on the lattice site, which result in shrinking of the unit cell. D'Ippolito et al. [17] has shown that the E_g peak shift to higher wavenumber as the T_d ion decrease in size.

3.3. Fourier-transform infrared spectroscopy

The FTIR spectra of the $x \geq 2$ samples is shown in Fig. 5. It is well known that infrared spectra of spinels are characterized by absorption band in the range between 400 -700 cm^{-1} [17,20]. The result shows that there are four bands at 479, 547, 656 and 803 cm^{-1}. The three low occurring frequency bands at 479, 547, and 656 cm^{-1} are attributed to the vibration modes of normal $ZnAl_2O_4$ spinel. Several studies have attributed them to the following vibration modes: Zn-O, Al-O and Zn-O-Al vibration [51–53]. These peaks are through-out the entire ZAOT samples because they all contain $ZnAl_2O_4$ phase as observed on the XRD and Raman results. The additional absorption band at 803 cm^{-1}, which is clearly noticeable from $x \geq 3$ can be attributed to the Al-O bond arising from Al in the T_d site of $ZnAl_2O_4$ (i.e. AlO_4). These results are in line with those of da Silva et al. [54] observed during the different annealing temperature of $ZnAl_2O_4$ showing the change of Al^{3+} site occupation.

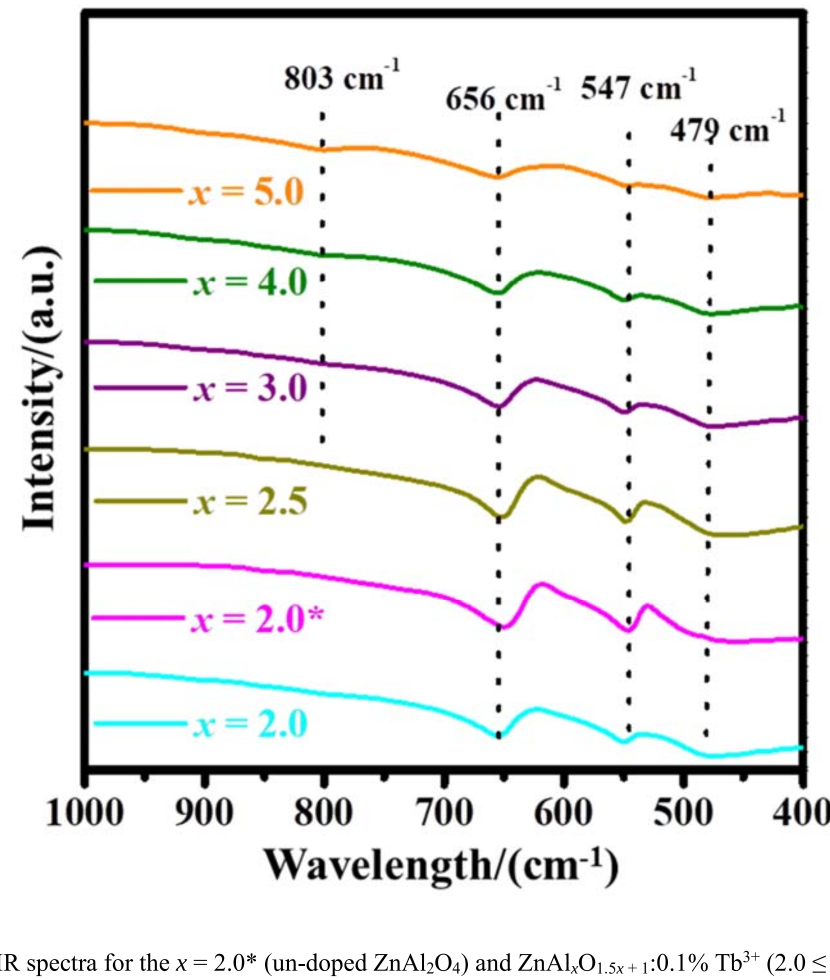

Fig. 5 The FTIR spectra for the $x = 2.0$* (un-doped $ZnAl_2O_4$) and $ZnAl_xO_{1.5x+1}$:0.1% Tb^{3+} ($2.0 \leq x \leq 5.0$).

3.4.Energy-dispersive X-ray spectroscopy

The EDS technique was deployed to analyse the chemical composition of the un-doped and ZAOT nano-powders and the spectra for the selected is shown on Fig. S4. The expected elements namely Zn, Al, and O are observed in all spectra. Except for the element Tb, due to its low doping concentration. The additional peak of carbon (C) observed at the lower energy is due to the sample coating or substrate carbon black during the sample preparation and measurement for the EDS spectrum.

3.5. Scanning Electron Microscopy

The SEM micrographs of the selected samples are shown on Fig. 6. The micrograph displayed on Fig. 6 (a) shows the morphology of x = 2.0 (un-doped) illustrating the presence of spherical particles can be attributed to the $ZnAl_2O_4$ since it is observed in all samples as shown on Fig. 6 (a) – (c). It is also clear that Tb^{3+} doping and varying the Al_x moles does not significantly influence the morphology of the prepared samples.

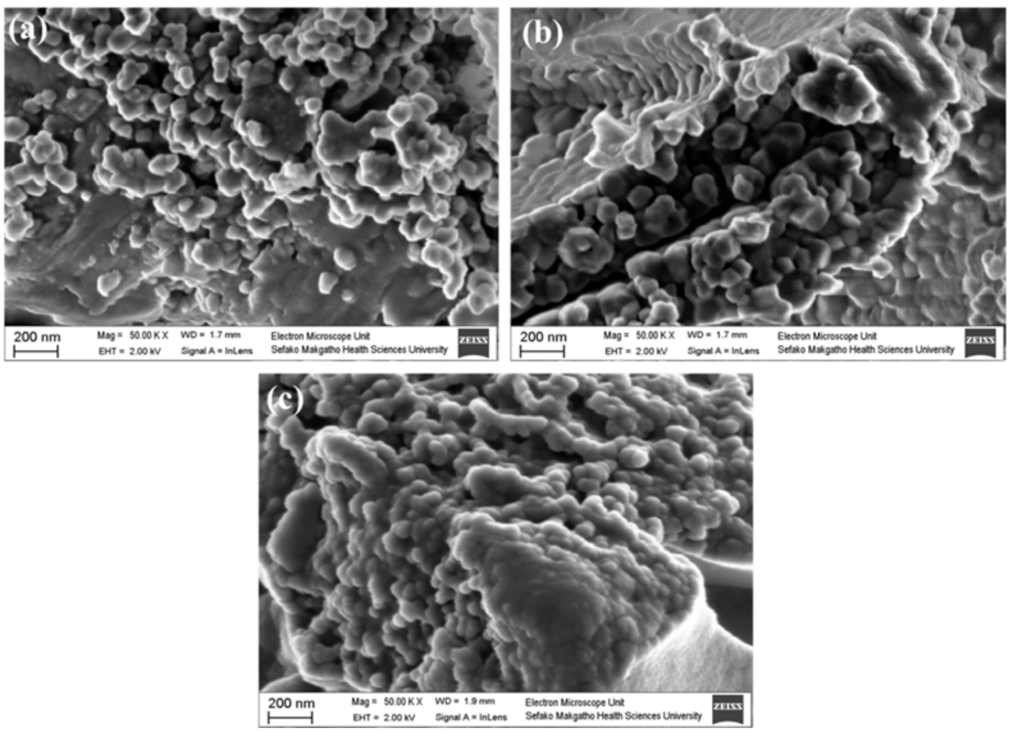

Fig. 6 The SEM micrographs of the (a) 2.0* (un-doped $ZnAl_2O_4$), (b) 2.0, and (c) 4.0 nanophosphor.

3.6.Transmission Electron Microscopy

The EDS and SEM selected samples were further analysed by the TEM to investigate the crystal sizes and shapes. The TEM images of the selected samples are shown in Fig. 7. In general, the TEM images confirm what has been observed on SEM in terms of the presence of irregular sphere of $ZnAl_2O_4$. The average crystallites size of the investigated prepared samples is in nanometer range (i.e. below 30 nm), which agrees very well with the XRD results.

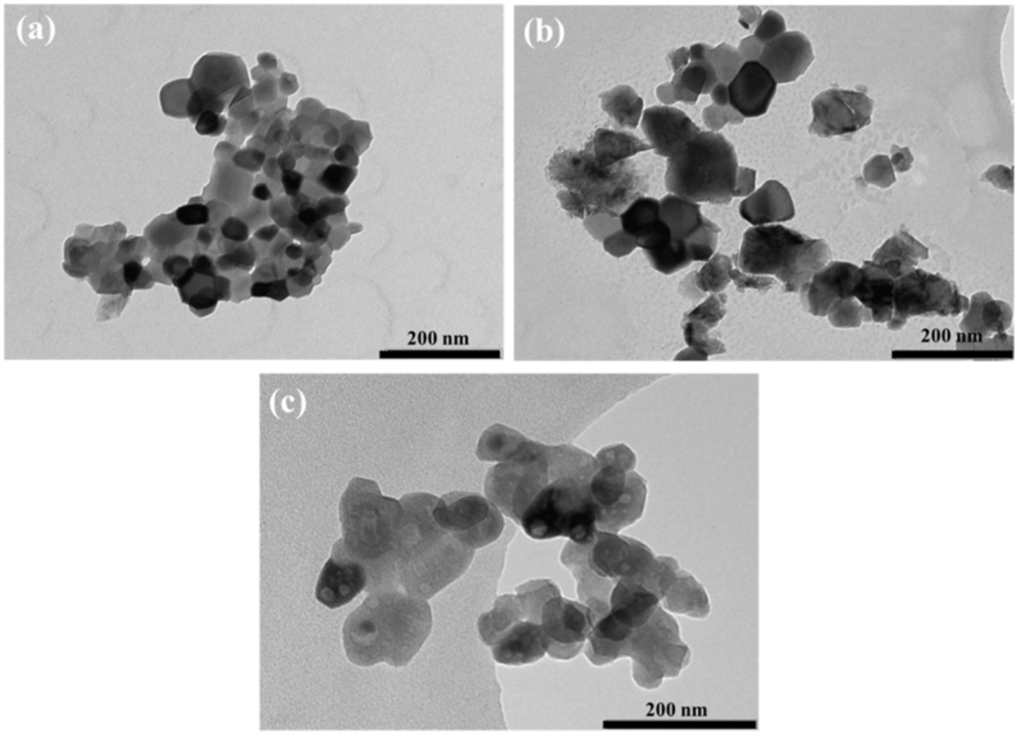

Fig. 7 The TEM micrographs of the (a) 2.0* (un-doped $ZnAl_2O_4$), (b) 2.0, and (c) 4.0 nanophosphor.

3.7.Photoluminescence spectroscopy

The room temperature PL emission spectra excited at various exitation wavelength in a range of 200 – 280 nm for the $ZnAl_xO_{1.5x+1}$:0.1% Tb^{3+} (x = 2.0) sample is illustrated in Fig. 8 (a). The emission spectra show the presence of eight emission peaks located at around 382, 414, 439, 458, 489, 545, 585 and 621 nm, which can be attributed to the $^5D_3 \rightarrow {}^7F_6$, $^5D_3 \rightarrow {}^7F_5$, $^5D_3 \rightarrow {}^7F_4$, $^5D_3 \rightarrow {}^7F_2$, $^5D_4 \rightarrow {}^7F_6$, $^5D_4 \rightarrow {}^7F_5$, $^5D_4 \rightarrow {}^7F_4$ and $^5D_4 \rightarrow {}^7F_3$ transitions of Tb^{3+} [23,30,55–57], respectively. The usual emissions at 398 nm from the $ZnAl_2O_4$ host was not detected and this might be due to the high annealing temparature used in this study which quenched the luminescence active traps within the $ZnAl_2O_4$ [26]. Singh et al. [26] showed that the luminescence active defects within $ZnAl_2O_4$ decreases dramatically after the anneallling temperature of 600 ºC. The emission intensity of the most intense peak at 545 nm as a function of excitation wavelength is shown on Fig. 8 (b), which shows a Gaussian behaviour and reveal that the optimum excitation wavelength is at 225 nm. This could be a good reason why a similar excitation wavelength of 228 nm was used to excite the $ZnAl_2O_4$:4 mol. % Tb^{3+} system, which were prepared via solution combustion method [57].

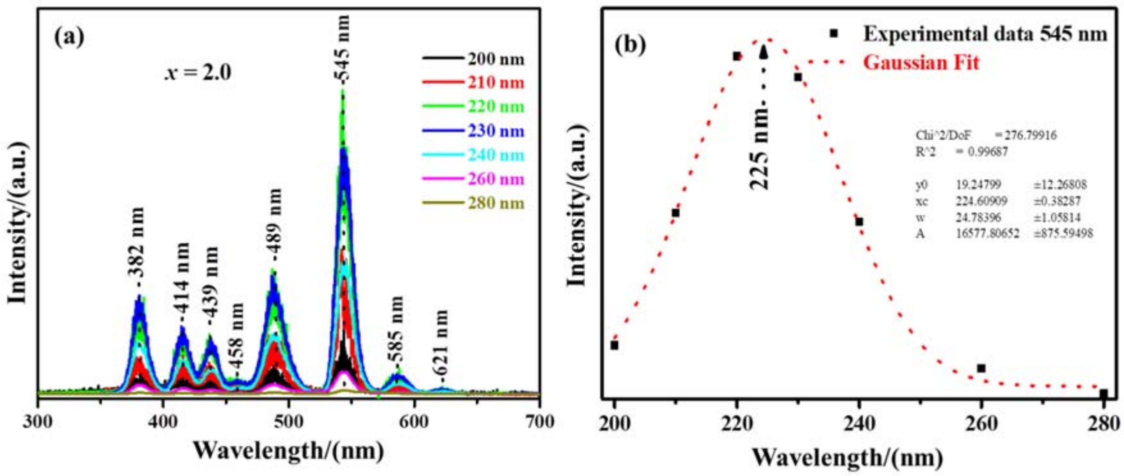

Fig. 8 The (a) emission spectra of the $ZnAl_xO_{1.5x+1}$:0.1% Tb^{3+} (x = 2.0) sample excited at various excitation wavelength and (b) emission intensity of the most intense peak (545 nm) as a function of excitation wavelength.

The room temperature PL excitation and emission spectra of the x = 2.0* (un-doped $ZnAl_2O_4$) and ZAOT series are presented in Fig. 9 (a). The excitation spectra of the doped (x = 2.0) displayed in Fig. 9 (a) were measured when monitoring the 545 nm emission which shows the presences of the prominent excitation band located at around 225 nm. This excitation band at 225 nm can be attributed to the spin allowed transition ($\Delta S = 0$) from the $4F^8$ (ground state) → $4F^7 5d^1$ of the Tb^{3+} ions [30,57]. The emission spectra show the presences of eight peaks which were like those observed on Fig. 8 (a). For the undoped (x = 2.0*) sample shown in Fig. 9 (a), it is important to point it out that the excitation was found when monitoring an emission at 458 nm. To further investigate the origin of the observed emissions, the emission spectra of both the x = 2.0 and un-doped (x = 2.0*) samples was normalized as shown in Fig. 9 (b). The excitation band at 267 nm is most likely to be due to the band-to-band transition of AlO_6 anion grouping in $ZnAl_2O_4$ [58]. To clearly mark the difference between the excitation and emission spectra, the line breaks on the horizontal axis and dotted vertical lines have been used. Fig. 9 (c) shows the deconvolution emission spectra of the un-doped (x = 2.0*) sample excited at 265 nm. The results shows that there are three emission bands located at around 407, 458, and 548 nm. These emission bands are ascribed to the $ZnAl_2O_4$ (host) intrinsic intraband gap defects, such as oxygen vacancies (Vo*) [54,58]. The excitation and emission spectrums of the ZAOT series is shown on Fig. 9 (d). The results show that there were no new emission peaks which were observed except the ones discussed in Figs. 8 (a) and 9 (a). Fig. 9 (e) shows the normalised emission intensity of the ZAOT series, it can be easily seen that the emission peak is similar to those in Figs. 8 and 9.

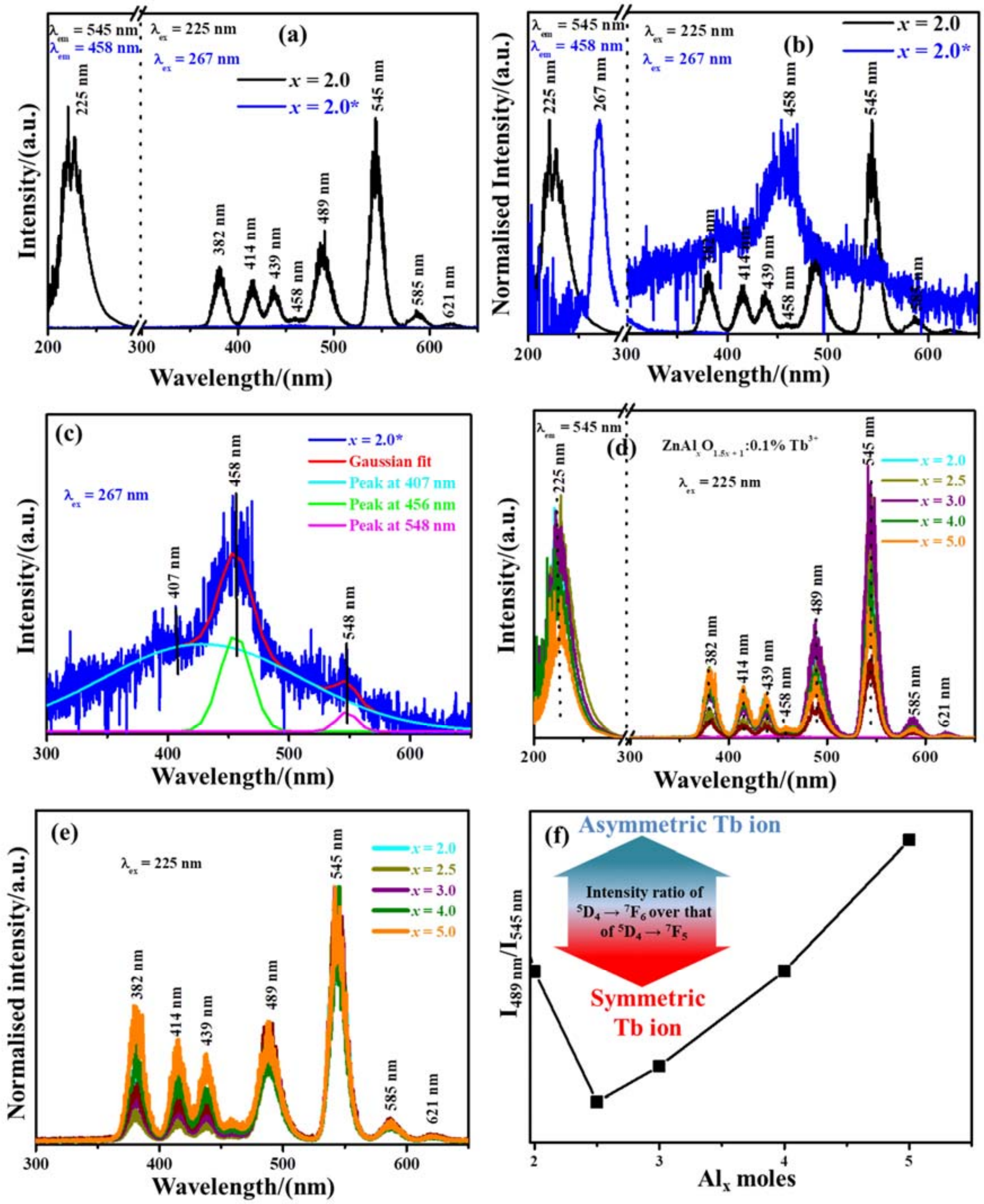

Fig. 9 Excitation and emission spectra of the (a) un-doped (x = 2.0*) and doped (x = 2.0), (b) normalized excitation and emission of un-doped and doped; and (c) deconvolution of the un-doped emission spectra. (d) Excitation and emission spectra and (e) normalised emission of the $ZnAl_xO_{1.5x+1}$:0.1% Tb^{3+} ($2.0 \leq x \leq 5.0$), and (f) emission intensity ration for the Tb^{3+} emission at 489 nm to 545 nm.

Since the Tb^{3+} ion can be present in the host material at various crystal field environment and the decrease and increase in $^5D_4 \rightarrow {}^7F_6$ transition emission intensity depends on the symmetry of the crystal field. In asymentric enviroment the intensity of this peak is higher as compared to the symmetric enviroment and as a result this has an impact on the emission colour [24-28]. To investigate and estimate the Tb^{3+} environment or occupation on the host lattice site the $I_{489\ nm}/I_{545\ nm}$ as a function of Al_x moles is shown in Fig. 9 (f). The 545 nm emission peak attributed to the $^5D_4 \rightarrow {}^7F_5$ magnetic dipole transition hardly varies in the presents of crystal field strength, while the 489 nm ascribed to the $^5D_4 \rightarrow {}^7F_6$ electrical dipole is exceptional sensitive to the local environment and depends on the symmetry of the crystal field [30,59]. It can be seen that $ZnAl_2O_4$ has attained symmetric environment at $x = 2.5$ due to the formation of singly $ZnAl_2O_4$. When Al_x increase beyond $x \geq 2.5$ Tb^{3+} gradually moves to asymmetric environment due to the stabilization of $ZnAl_2O_4$ crystal structure. The variation in $I_{489\ nm}/I_{545\ nm}$ is in consistent with the XRD results in Fig. S1 (a). Therefore, it can be concluded that the Tb^{3+} environment is regulated by the Al_x moles.

The emission intensity of the most intense peak (545 nm) as a function of Al_x moles is shown on Fig. 10. The result shows an optimum emission intensity when $x = 2.5$, which can be simply attributed to the change in the crystal field environment (see Fig. 9 (f)) and the Tb^{3+} occupation in symmetric site within the cubic $ZnAl_2O_4$. That is when the Al^{3+} substitutes the Zn^{2+} in crystal lattice, which also causes the reduction on the unit cell. This result clearly shows that the emission intensity highly depends on the Al_x moles, Tb^{3+} environment and the phases present in the sample.

The proposed pathway channels for the excitation and emissions discussed in this paper are shown in Fig. 11. The energy level location of Tb^{3+} within $ZnAl_2O_4$ was predicted based on the Dorenbo's diagram [28,60].

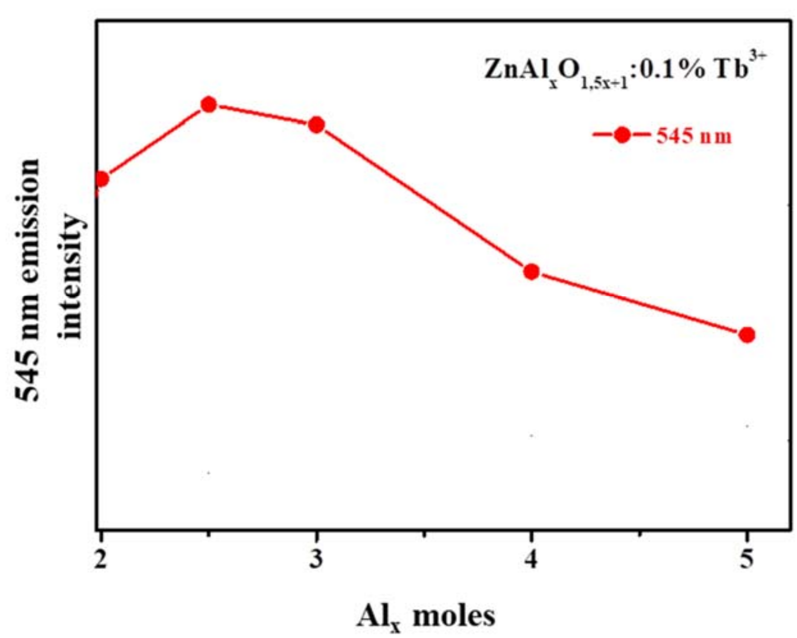

Fig. 10 Emission intensity of the 545 nm as a function of the Al_x moles.

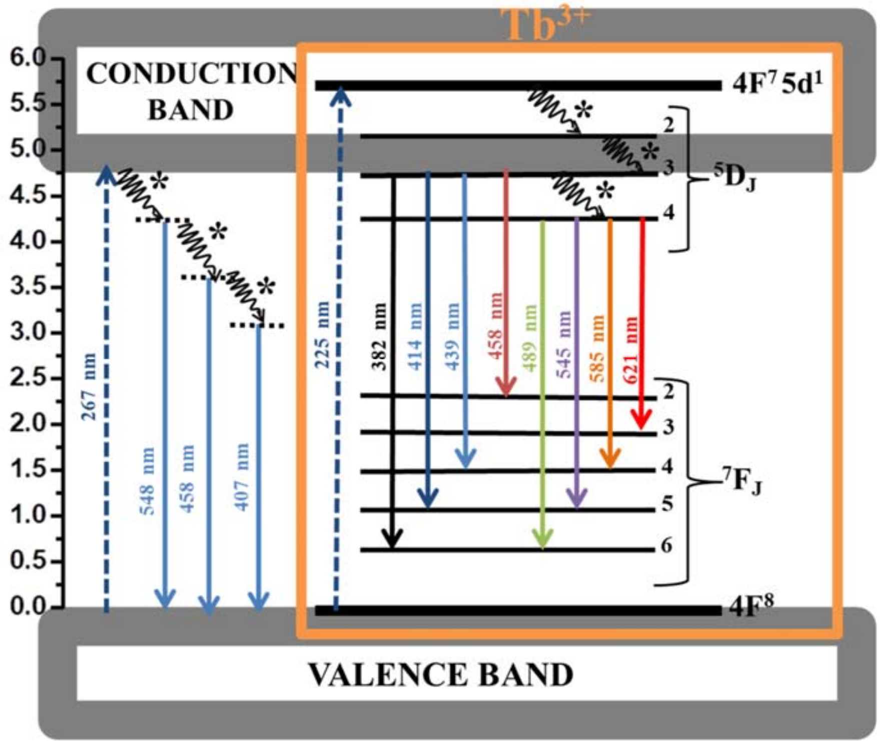

Fig. 11 The proposed excitation and emission pathways mechanism for the $ZnAl_2O_4$:0.1%Tb^{3+}.

3.8.Lifetime

Fig. 12 shows the RT phosphorescence lifetime of the prepared ZAOT series. The normalised decay curves shown in Fig. 12 was taken when monitoring the 545 nm emission and 225 nm excitation for the doped samples. For the undoped (x = 2.0*), the decay curve was taken when monitoring 458 nm emission and 267 nm excitation. All the samples where fitted using the first order exponential decay presented in equation 3 [28,41,61].

$$I(t) = A + Be^{(-t/\tau)} \quad \ldots (3)$$

where I represents the phosphorescent intensity, A is the background, B is the fitting parameters, t is the time of measurement and τ decay time values. The fitting parameter and decay times are presented in Table 2. As expected, the lifetime results are very similar for the doped samples and this is because the content of the Tb^{3+} in the sample is constant, while the Al_x contents was varied.

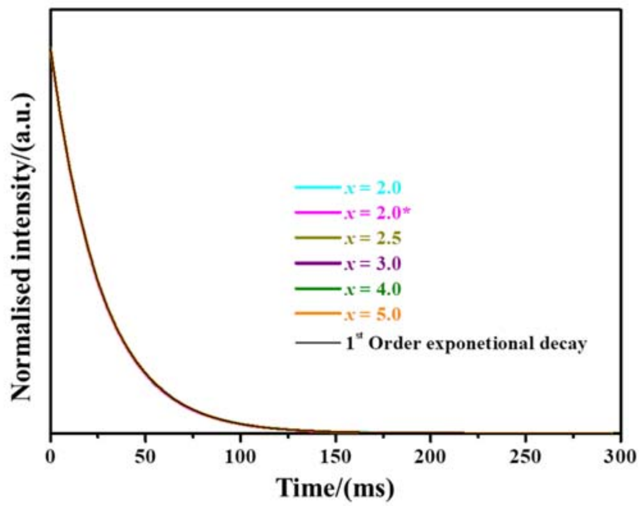

Fig. 12 The normalised decay curve of host at x = 2.0 and $ZnAl_xO_{1.5x+1}$:0.1%Tb^{3+} ($2.0 \leq x \leq 5.0$)

Table 2. Sample identification of fitting parameter, decay times and CIE colour coordinates.

Sample ID	**fitting parameter**	**decay times**	**CIE**
x	A_1	τ_1 **(ms)**	**(x;y)**
2.0	8493.06 ± 2.00	26.94 ± 0.01	(0.232;0.455)
2.0*	3309.75 ± 3.45	26.63 ± 0.04	(0.153;0.147)
2.5	7974.16 ± 1.77	26.89 ± 0.01	(0.243;0.531)
3.0	8096.12 ± 2.59	26.87 ± 0.01	(0.238;0.502)
4.0	7310.85 ± 1.80	26.85 ± 0.01	(0.223;0.429)
5.0	7814.12 ± 1.73	26.84 ± 0.01	(0.219;0.397)

* - denotes un-doped sample

3.9.Colour chromaticity

The International Commission on Illumination (CIE) chromaticity diagram with vertex region of different colour and the co-ordinates of the luminescent material are displayed on Fig. 13. The colour co-ordinates of the prepared sample were calculated using the CIE co-ordinate calculator software [62]. The colour co-ordinates for the x = 2.0 sample excited at different excitation wavelength is shown on Fig. 13 (a). The results show that the excitation wavelength influences the emission colour. Fig. 13 (b) compares the emission colour co-ordinates of the un-dope (x = 2.0*) and $ZnAl_2O_4$:0.1% Tb^{3+} dope sample. The un-doped (x = 2.0*) sample shows a blue colour emission while the Tb^{3+} doped shows the green emission, which clearly shows that doping influences the emission of the host material [57]. The colour co-ordinates for the ZAOT series is shown on Fig. 13 (c) and the (x;y) values are also presented in Table 2. The results clearly show that varying the Al_x moles influence the emission colour due to the changing crystal field environment of the Tb^{3+} induced by varying Al_x moles. The emission colour could be tuned from greenish to bluish. Fig. 13 (d) shows the CIE colour co-ordinates for the $x = 2.5$ sample when excited at 225 and 308 nm. The results show that the emission colour highly depends on the excitation wavelength.

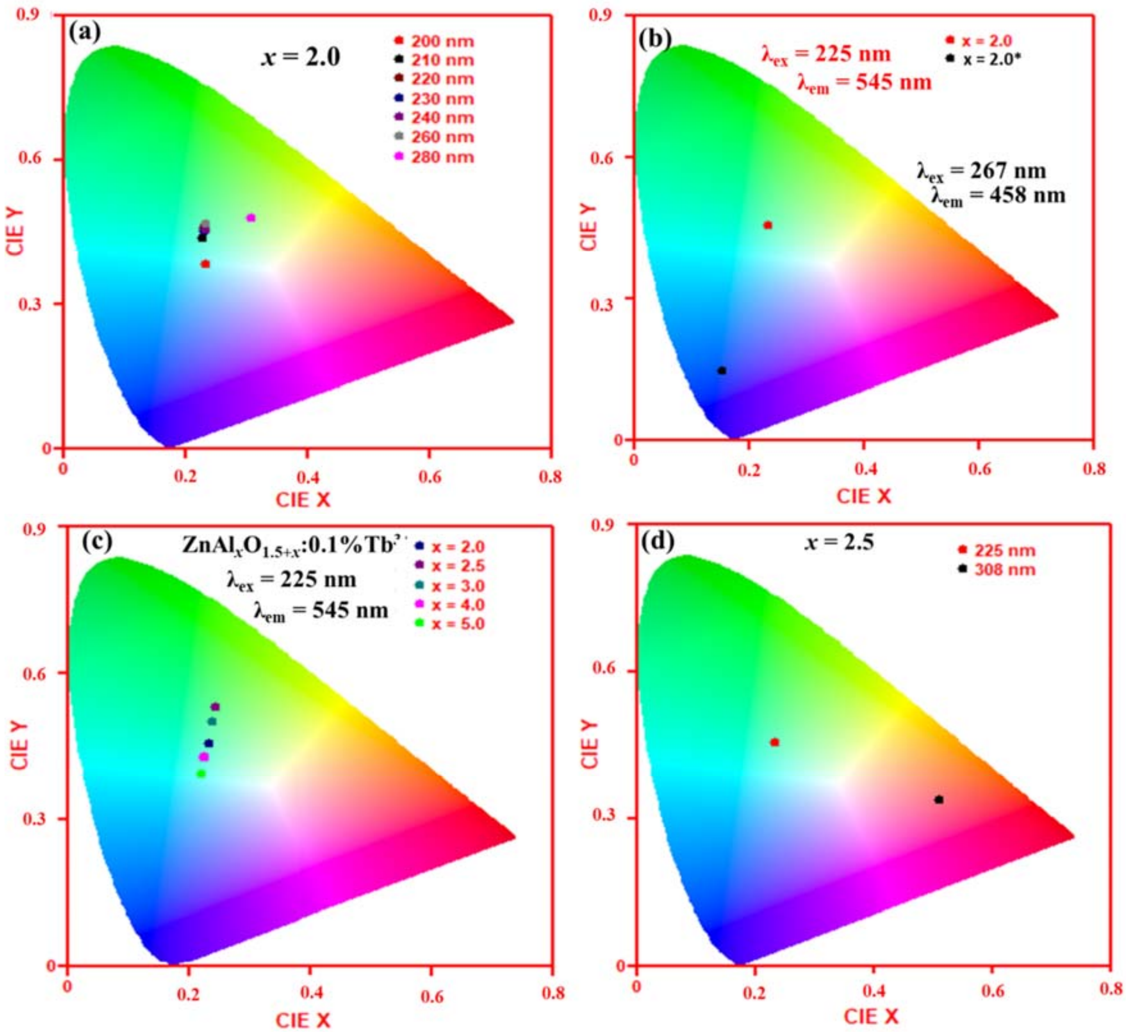

Fig. 13 CEI colour for the (a) $x = 2.0$ at various excitation wavelength, (b) Tb^{3+} doped and un-doped ($x = 2.0$*) sample at $x = 2.0$, (c) ZAOT series, and (d) $x = 2.5$ at the excitation wavelength of 225 and 308 nm.

4. Conclusion

In summary, ZAOT nano-powders were successfully synthesized via citrate sol-gel method. The XRD shows the presence of both ZnO and $ZnAl_2O_4$ phases on the prepared materials, which highly depends on the Al_x moles. The SEM showed that varying the Al_x moles does not significantly influence the morphology of the prepared nanophosphor. The PL emission spectra showed a maximum of eight emission peaks which were attributed to the ^5D_j (j = 3 and 4) → ^7F_j (j = 3 - 6) from Tb^{3+} emission. The PL emission colour and intensity depends on the crystal field and Tb^{3+} environment within the $ZnAl_2O_4$ matrix, which is regulated by the Al_x moles. The lifetime measurement for the 545 nm showed that the prepared nano-powders have similar decay mechanism despite different crystal environment of Tb^{3+}. CIE colour chromaticity showed that varying Al_x moles and excitation wavelength significantly influence the emission colour.

Declaration

Not applicable.

Acknowledgements

The author would also like to acknowledge Miss. N. Thabane for assisting in sample synthesis. Dr James Wesley-Smith at Electron Microscopy Unit at Sefako Makgatho Health Science University is acknowledged for the SEM and TEM imaging.

References

1. Lahmer MA. The effect of Fe-doping on the electronic, optical and magnetic properties of $ZnAl_2O_4$; a first-principles study. *Comput Condens Matter*. 2019;20:e00387. doi:10.1016/j.cocom.2019.e00387

2. Cady CW, Gardner G, Maron ZO, et al. Tuning the electrocatalytic water oxidation properties of AB_2O_4 spinel nanocrystals: A (Li, Mg, Zn) and B (Mn, Co) site variants of $LiMn_2O_4$. *ACS Catal*. 2015;5(6):3403-3410. doi:10.1021/acscatal.5b00265

3. Yan G, Li G, Tan H, Gu Y, Li Y. Spinel-type ternary multimetal hybrid oxides with porous hierarchical structure grown on Ni foam as large-current-density water oxidation electrocatalyst. *J Alloys Compd*. 2020;838. doi:10.1016/j.jallcom.2020.155662

4. Masmali NA, Osman Z, Arof AK. Recent developments in zinc-based two-cation oxide spinels: From synthesis to applications. *Ceram Int*. Published online October 2020. doi:10.1016/j.ceramint.2020.09.249

5. Kulkarni P, Balkrishna RG, Ghosh D, et al. Molten salt synthesis of $CoFe_2O_4$ and its energy storage properties. *Mater Chem Phys*. 2021;257. doi:10.1016/j.matchemphys.2020.123747

6. Song K, Chen X, Yang R, et al. Novel hierarchical $CoFe_2Se_4$@$CoFe_2O_4$ and $CoFe_2S_4$@$CoFe_2O_4$ core-shell nanoboxes electrode for high-performance electrochemical energy storage. *Chem Eng J*. 2020;390. doi:10.1016/j.cej.2020.124175

7. Melato LT, Ntwaeaborwa OM, Kroon RE, Motaung TE, Motloung S V. Effect of

Ho3+ concentration on the structure, morphology and optical properties of $Ba_{0.5}Mg_{0.5}Al_2O_4$ nanophosphor. *J Mol Struct*. 2019;1176:217-225. doi:10.1016/j.molstruc.2018.08.093

8. Malimabe MA, Motloung S V., Motaung TE, Koao LF. Effects of Eu^{3+} co-doping on the structural and optical properties of Ce^{3+} doped ZnO powder synthesized by chemical bath deposition method. *Phys B Condens Matter*. 2020;579. doi:10.1016/j.physb.2019.411890

9. Maphiri VM, Wesley-Smith J, Motloung S V. Phase transition and optical properties of $Ba_{1-x}Zn_xAl_2O_4$:0.1% Eu^{3+} prepared via citrate sol-gel method. *J Lumin*. 2019;215(February):116710. doi:10.1016/j.jlumin.2019.116710

10. Jiang FX, Tong RX, Yan Z, Ji LF, Xu XH. d-electron-dependent transparent conducting oxide of V-doped ZnO thin films. *J Alloys Compd*. 2020;822. doi:10.1016/j.jallcom.2020.153706

11. Sarma BK, Rajkumar P. Al-doped ZnO transparent conducting oxide with appealing electro-optical properties – Realization of indium free transparent conductors from sputtering targets with varying dopant concentrations. *Mater Today Commun*. 2020;23:100870. doi:10.1016/j.mtcomm.2019.100870

12. Miron I, Enache C, Vasile M, Grozescu I. Optical properties of $ZnAl_2O_4$ nanomaterials obtained by the hydrothermal method. *Phys Scr*. 2012;2012(T149):014064. doi:10.1088/0031-8949/2012/T149/014064

13. Atiq S, Ansar MT, Hassan A, et al. Interlayer effect on photoluminescence enhancement and band gap modulation in Ga-doped ZnO thin films. *Superlattices Microstruct*. 2020;144. doi:10.1016/j.spmi.2020.106576

14. Hussain T, Junaid M, Atiq S, et al. Tunable dielectric behaviour and energy band gap range of $ZnAl_2O_4$ ceramics mediated by Mg substitution. *J Alloys Compd*. 2017;724:940-950. doi:10.1016/j.jallcom.2017.07.104

15. Maphiri VM, Dejene FB, Motloung S V. Effects of Mg^{2+} concentration on the structure and optical properties of $Mg_xAl_2O_{3+x}$:0.88% Cd^{2+} ($0.25 \leq x \leq 4.5$) nano-powders synthesized via citrate sol-gel. *Results Phys*. 2017;7:3510-3521. doi:10.1016/j.rinp.2017.09.019

16. Kroon RE, Tabaza WAI, Swart HC. Luminescence of $(Mg,Zn)Al_2O_4$:Tb mixed spinel thin films prepared by spin-coating. In: Jiang S, Digonnet MJF, eds. *Optical Components and Materials XII*. Vol 9359. SPIE; 2015:93591K. doi:10.1117/12.2077585

17. D'Ippolito V, Andreozzi GB, Bersani D, Lottici PP. Raman fingerprint of chromate, aluminate and ferrite spinels. *J Raman Spectrosc*. 2015;46(12):1255-1264. doi:10.1002/jrs.4764

18. Nasr M, Viter R, Eid C, et al. Synthesis of novel $ZnO/ZnAl_2O_4$ multi co-centric nanotubes and their long-term stability in photocatalytic application. *RSC Adv*. 2016;6(105):103692-103699. doi:10.1039/c6ra22623j

19. Wang J, Wang A, Hu D, Wu X, Liu Y, Chen T. Synthesis, characterization and

properties of Ni^{2+}-doped $ZnAl_2O_4$-based spinel-type solid acid catalysts: $SO_4^{2-}/Zn_{1-x}Ni_xAl_2O_4$. *Mater Chem Phys*. 2020;239:122319. doi:10.1016/j.matchemphys.2019.122319

20. Mohaček-Grošev V, Vrankić M, Maksimović A, Mandić V. Influence of titanium doping on the Raman spectra of nanocrystalline $ZnAl_2O_4$. *J Alloys Compd*. 2017;697:90-95. doi:10.1016/j.jallcom.2016.12.116

21. Feng X, Huang Y, Chen X, Wei C, Zhang X, Chen M. Hierarchical $CoFe_2O_4/NiFe_2O_4$ nanocomposites with enhanced electrochemical capacitive properties. *J Mater Sci*. 2018;53(4):2648-2657. doi:10.1007/s10853-017-1735-9

22. Peng C, Li G, Geng D, Shang M, Hou Z, Lin J. Fabrication and luminescence properties of one-dimensional $ZnAl_2O_4$ and $ZnAl_2O_4$: A^{3+} (A = Cr, Eu, Tb) microfibers by electrospinning method. *Mater Res Bull*. 2012;47(11):3592-3599. doi:10.1016/j.materresbull.2012.06.056

23. Lakshminarayana G, Wondraczek L. Photoluminescence and energy transfer in Tb^{3+}/Mn^{2+} co-doped $ZnAl_2O_4$ glass ceramics. *J Solid State Chem*. 2011;184(8):1931-1938. doi:10.1016/j.jssc.2011.05.059

24. Rusu E, Ursaki V, Novitschi G, Vasile M, Petrenco P, Kulyuk L. Luminescence properties of $ZnGa_2O_4$ and $ZnAl_2O_4$ spinels doped with Eu^{3+} and Tb^{3+} ions. *Phys status solidi*. 2009;6(5):1199-1202. doi:10.1002/pssc.200881172

25. Motloung SV, Kumari P, Koao LF, Motaung TE, Hlatshwayo TT, Mochane MJ. Effects of annealing time on the structure and optical properties of $ZnAl_2O_4$/ZnO prepared via citrate sol-gel process. *Mater Today Commun*. 2018;14:294-301. doi:10.1016/j.mtcomm.2018.02.004

26. Singh V, Singh N, Pathak MS, Dubey V, Singh PK. Annealing effects on the luminescence properties of Ce doped $ZnAl_2O_4$ produced by combustion synthesis. *Optik (Stuttg)*. 2018;155:285-291. doi:10.1016/j.ijleo.2017.10.167

27. Linganna K, Ju S, Basavapoornima C, Venkatramu V, Jayasankar CK. Luminescence and decay characteristics of Tb^{3+}-doped fluorophosphate glasses. *J Asian Ceram Soc*. 2018;6(1):82-87. doi:10.1080/21870764.2018.1442674

28. Motloung S V., Tshabalala KG, Kroon RE, Hlatshwayo TT, Mlambo M, Mpelane S. Effect of Tb^{3+} concentration on the structure and optical properties of triply doped $ZnAl_2O_4$:1% Ce^{3+},1% Eu^{3+},x% Tb^{3+} nano-phosphors synthesized via citrate sol-gel method. *J Mol Struct*. 2019;1175:241-252. doi:10.1016/j.molstruc.2018.08.002

29. Motloung S V., Tsega M, Dejene FB, et al. Effect of annealing temperature on structural and optical properties of $ZnAl_2O_4$:1.5% Pb^{2+} nanocrystals synthesized via sol-gel reaction. *J Alloys Compd*. 2016;677:72-79. doi:10.1016/j.jallcom.2016.03.170

30. Kumar M, Gupta SK. An insight into optical spectroscopy of intense green emitting $ZnAl_2O_4:Tb^{3+}$ nanoparticles: Photo, thermally stimulated luminescence and EPR study. *J Lumin*. 2015;168:151-157. doi:10.1016/j.jlumin.2015.07.021

31. Jain M, Manju, Gundimeda A, et al. Defect induced broadband visible to near-infrared luminescence in $ZnAl_2O_4$ nanocrystals. *Appl Surf Sci*. 2019;480:945-950.

doi:10.1016/j.apsusc.2019.02.198

32. Kumari P, Dwivedi Y. Structural and photophysical investigations of bright yellow emitting Dy: $ZnAl_2O_4$ nanophosphor. *J Lumin*. 2016;178:407-413. doi:10.1016/j.jlumin.2016.06.027

33. Wang SF, Sun GZ, Fang LM, Lei L, Xiang X, Zu XT. A comparative study of $ZnAl_2O_4$ nanoparticles synthesized from different aluminum salts for use as fluorescence materials. *Sci Rep*. 2015;5. doi:10.1038/srep12849

34. Motloung S V., Dejene FB, Swart HC, Ntwaeaborwa OM. Effects of Zn/citric acid mole fraction on the structure and luminescence properties of the un-doped and 1.5% Pb^{2+} doped $ZnAl_2O_4$ powders synthesized by citrate sol-gel method. *J Lumin*. 2015;163:8-16. doi:10.1016/j.jlumin.2015.02.027

35. Mphelane MN, Mhlongo MR, Motaung TE, Koao LF, Hlatshwayo TT, Motloung SV. Effects of annealing temperature on the structure and photoluminescence properties of the $ZnO/ZnAl_2O_4/Ca_5Al_6O_{14}/Ca_3Al_4ZnO_{10}$:0.1% Ce^{3+} mixed-phases nanophosphor prepared by citrate sol–gel process. *Appl Phys A*. 2020;126(10):1-11. doi:10.1007/s00339-020-04002-6

36. Chen JC, Tang CT. Preparation and application of granular ZnO/Al_2O_3 catalyst for the removal of hazardous trichloroethylene. *J Hazard Mater*. 2007;142(1-2):88-96. doi:10.1016/j.jhazmat.2006.07.061

37. Takemoto T, He D, Teng Y, Tabata K, Suzuki E, Suzuki E. Enhancement of methanol selectivity in the products of direct selective oxidation of methane in CH_4-O_2-NO with Cu-ZnO/Al_2O_3. *J Catal*. 2001;198(1):109-115. doi:10.1006/jcat.2000.3119

38. Fang Z, Wang H, Liu J, Ouyang L, Zhu M. Effect of scandium and zirconium alloying on microstructure and gaseous hydrogen storage properties of YFe_3. *J Rare Earths*. 2022;40(3):467-472. doi:10.1016/j.jre.2020.11.015

39. Wang R, Tian X, Yao Z, Zhao X, Hao H. Influence of rare earth element terbium doping on microstructure and magnetostrictive properties of $Fe_{81}Al_{19}$ alloy. *J Rare Earths*. 2022;40(3):451-456. doi:10.1016/j.jre.2020.12.009

40. Chew KY, Bakar MA, Abu Bakar NHH. Synthesis of Barium Nickel Titanium Oxide Stabilized by Citric Acid. *Model Numer Simul Mater Sci*. 2013;03(01):23-27. doi:10.4236/mnsms.2013.31b007

41. Maphiri VM, Dwivedi Y, Koao LF, Kroon RE, Motloung S V. Analysis of varying Gd^{3+} concentrations on the structure and optical properties of $ZnAl_2O_4$:0.1% Eu^{3+}; x% Gd^{3+} ($0 \leq x \leq 1.2$) synthesized via citrate sol–gel method. *Appl Phys A Mater Sci Process*. 2020;126(1). doi:10.1007/s00339-019-3260-y

42. Magomedov MN. On the deviation from the Vegard's law for the solid solutions. *Solid State Commun*. 2020;322. doi:10.1016/j.ssc.2020.114060

43. Foronda HM, Mazumder B, Young EC, et al. Analysis of Vegard's law for lattice matching $In_xAl_{1-x}N$ to GaN by metalorganic chemical vapor deposition. *J Cryst Growth*. 2017;475:127-135. doi:10.1016/j.jcrysgro.2017.06.008

44. Shahmirzaee M, Shafiee Afarani M, Arabi AM, Iran Nejhad A. In situ crystallization

of $ZnAl_2O_4/ZnO$ nanocomposite on alumina granule for photocatalytic purification of wastewater. *Res Chem Intermed*. 2017;43(1):321-340. doi:10.1007/s11164-016-2624-6

45. Rani G. Annealing effect on the structural, optical and thermoluminescent properties of $ZnAl_2O_4:Cr^{3+}$. *Powder Technol*. 2017;312:354-359. doi:10.1016/j.powtec.2017.02.040

46. Mulwa WM, Dejene BF, Onani MO, Ouma CNM. Effect of Cu^{2+} doping on the structural, electronic and optical properties of $ZnAl_2O_4$: A combined experimental and DFT+U study. *J Lumin*. 2017;184:7-16. doi:10.1016/j.jlumin.2016.12.008

47. Patterson AL. The Scherrer Formula for X-Ray Particle Size Determination. *Phys Rev*. 1939;56(10):978. doi:10.1103/PhysRev.56.978

48. Williamson GK, Hall WH. X-RAY LINE BROADENING FROM FILED ALUMINIUM AND WOLFRAM*. *Acta Metall*. 1953;1(1):22-31.

49. Modi KB, Raval PY, Shah SJ, et al. Raman and Mossbauer Spectroscopy and X-ray Diffractometry Studies on Quenched Copper–Ferri–Aluminates. *Inorg Chem*. 2015;54(4):1543-1555. doi:10.1021/ic502497a

50. Song Y, Zhang S, Zhang C, Yang Y, Lv K. Raman Spectra and Microstructure of Zinc Oxide irradiated with Swift Heavy Ion. *crystals*. Published online 2019. doi:10.3390/cryst9080395

51. Kirankumar VS, Sumathi S. Catalytic activity of bismuth doped zinc aluminate nanoparticles towards environmental remediation. *Mater Res Bull*. 2017;93:74-82. doi:10.1016/j.materresbull.2017.04.022

52. Zhu Z, Li X, Zhao Q, Liu S, Hu X, Chen G. Facile solution synthesis and characterization of porous cubic-shaped superstructure of $ZnAl_2O_4$. *Mater Lett*. 2011;65(2):194-197. doi:10.1016/j.matlet.2010.09.085

53. Li X, Zhu Z, Zhao Q, Wang L. Photocatalytic degradation of gaseous toluene over $ZnAl_2O_4$ prepared by different methods: A comparative study. *J Hazard Mater*. 2011;186(2-3):2089-2096. doi:10.1016/j.jhazmat.2010.12.111

54. Da Silva AA, Gonçalves AS, Davolosv MR, Santagneli SH. Al^{3+} environments in nanostructured $ZnAl_2O_4$ and their effects on the luminescence properties. *J Nanosci Nanotechnol*. 2008;8(11):5690-5695. doi:10.1166/jnn.2008.218

55. Som S, Sharma SK, Lochab SP. Swift heavy ion induced structural and optical properties of $Y_2O_3:Eu^{3+}$ nanophosphor. *Mater Res Bull*. 2013;48(2):844-851. doi:10.1016/j.materresbull.2012.11.079

56. Matsushita AFY, Pais AACC, Valente AJM. Energy transfer and multicolour tunable emission of Eu,Tb(PSA)Phen composites. *Colloids Surfaces A Physicochem Eng Asp*. 2019;569:93-101. doi:10.1016/j.colsurfa.2019.02.049

57. Tshabalala KG, Nagpure IM, Swart HC, Ntwaeaborwa OM, Cho S-H, Park J-K. Enhanced green emission from UV down-converting Ce^{3+} –Tb^{3+} co-activated $ZnAl_2O_4$ phosphor . *J Vac Sci Technol B, Nanotechnol Microelectron Mater Process Meas Phenom*. 2012;30(3):031401. doi:10.1116/1.3696720

58. Motloung S V., Dejene FB, Ntwaeaborwa OM, Swart HC. Effects of catalyst/zinc mole fraction on $ZnAl_2O_4$:0.01% Cr^{3+} nanocrystals synthesized using sol-gel process. *Mater Res Express*. 2015;1(4). doi:10.1088/2053-1591/1/4/045029

59. Gupta SK, Ghosh PS, Arya A, Natarajan V. Origin of blue emission in ThO2 nanorods: Exploring it as a host for photoluminescence of Eu^{3+}, Tb^{3+} and Dy^{3+}. *RSC Adv*. 2014;4(93):51244-51255. doi:10.1039/c4ra09681a

60. Dorenbos P. Electronic structure engineering of lanthanide activated materials. *J Mater Chem*. 2012;22(42):22344-22349. doi:10.1039/c2jm34252a

61. Eldridge JI. Luminescence decay-based Y_2O_3:Er phosphor thermometry: Temperature sensitivity governed by multiphonon emission with an effective phonon energy transition. *J Lumin*. 2019;214:116535. doi:10.1016/j.jlumin.2019.116535

62. ⟨http://www.mathworks.com/matlabcentral/fileexchange/29620-cie-coordi nate-calculator⟩ 2012 (accessed 21.10.12).